

# **Three-Dimensional Fibril-Reinforced Finite Element Model of Articular Cartilage**

**L.P. Li<sup>a,\*</sup>, J.T.M. Cheung<sup>b</sup> and W. Herzog<sup>b</sup>**

<sup>a</sup> Department of Mechanical and Manufacturing Engineering, University of Calgary;

<sup>b</sup> Human Performance Laboratory, Faculty of Kinesiology, University of Calgary;

2500 University Drive, N.W., Calgary, Alberta, Canada T2N 1N4

\*Corresponding author:

LePing Li, Ph.D.

Department of Mechanical and Manufacturing Engineering

University of Calgary

2500 University Drive, N.W.

Calgary, Alberta, Canada T2N 1N4

Email: [Leping.Li@ucalgary.ca](mailto:Leping.Li@ucalgary.ca)

1 ABSTRACT

2 Collagen fiber orientations in articular cartilage are tissue depth-dependent and joint site-specific.  
3 A realistic three-dimensional (3D) fiber orientation has not been implemented in modeling fluid  
4 flow-dependent response of articular cartilage, thus the detailed mechanical role of the collagen  
5 network may have not been fully understood. In the present study, a previously developed fibril-  
6 reinforced model of articular cartilage was extended to account for the 3D fiber orientation. A  
7 numerical procedure for the material model was incorporated into the finite element code  
8 ABAQUS using the USER MATERIAL option. Unconfined compression and indentation testing  
9 were evaluated. For indentation testing, we considered a mechanical contact between a solid  
10 indenter and a medial femoral condyle, assuming fiber orientations in the surface layer to follow  
11 the split-line pattern. The numerical results from the 3D modeling for unconfined compression  
12 seemed reasonably to deviate from that of axisymmetric modeling. Significant fiber orientation  
13 dependence was observed in the displacement, fluid pressure and velocity for the cases of  
14 moderate strain-rates, or during early relaxation. The influence of fiber orientation diminished at  
15 static and instantaneous compressions.

16

17 **KEYWORDS:** Articular cartilage mechanics; Collagen fiber orientation; Fibril-reinforcement;  
18 Fluid pressure; Indentation

1 1. INTRODUCTION

2 The onset of osteoarthritis is believed to be associated with abnormal joint contact. Knowledge  
3 of the mechanics of articular cartilage may improve the understanding of mechanotransduction  
4 processes in the tissue that play important roles in the progression of joint disease [1]. Articular  
5 cartilage is anisotropic, inhomogeneous and nonlinear in nature. It consists of three major load-  
6 supporting constituents: the collagen fiber network, a negatively charged proteoglycan matrix and  
7 a fluid. Articular cartilage exhibits strong creep and relaxation behavior, and is often subjected to  
8 dynamic loading causing large deformation. These mechanical properties and loading conditions  
9 need to be considered when studying joint mechanics.

10 Many mathematical models of articular cartilage are based on the biphasic theory [2] which  
11 explains the time-dependent response of the tissue through interstitial fluid flow in the solid  
12 matrix. Some of these models include formulations of large deformation [3,4] and intrinsic  
13 viscoelasticity of the tissue matrix [5,6]. Transverse isotropy was introduced to account for some  
14 direction-dependent material behavior [7,8,9]. Viscoelasticity and hyperelasticity of the tissue  
15 matrix were also considered simultaneously to account for transverse isotropy and large  
16 deformation [10].

17 Collagen fiber reinforcement and the specific fiber orientation in cartilage have been  
18 identified as key factors in the tissue mechanical response [11,12,13] that is strongly strain-rate  
19 dependent [14,15]. Recent efforts have been made to model the nonlinear mechanical  
20 characteristics of cartilage governed by the collagen fibril reinforcement [16,17,18,19]. In these  
21 studies, articular cartilage was modeled as a fluid-saturated elastic solid reinforced by a nonlinear  
22 fibrillar network. These models were capable of describing the strong creep and relaxation  
23 behavior and compression-offset dependent stiffening of cartilage in unconfined compression and  
24 indentation, showing that the interplay between the nonlinear fibril reinforcement and fluid

1 pressurization determined the load response of cartilage [20,21]. Fibril-reinforced models could  
2 also account for the reaction force during swelling, confined compression, indentation and  
3 unconfined compression, and predict the lateral deformation during unconfined compression [19].  
4 However, all these model studies were limited to two dimensional or axisymmetric testing  
5 configurations. True 3D collagen configurations have not been implemented and they might  
6 affect solutions in non-intuitive ways.

7 Three dimensional geometrically accurate finite element joint contact models, such as for the  
8 knee, have been developed based on magnetic resonance or computed tomography imaging  
9 [22,23,24,25]. These finite element models have great potential for providing information of  
10 normal and pathological joint contact mechanics [26]. They have been employed for studying  
11 bioengineering questions, including the effects of PCL reconstruction [27], the rate of  
12 progression of knee osteoarthritis after ACL injury [28], meniscal tear and meniscectomy  
13 [29,30,31], and stress alterations due to cartilage defects [32]. For simplicity, articular cartilage  
14 was considered homogenous, isotropic and linearly elastic in these 3D knee models; and  
15 interstitial fluid flow was neglected. Because of the inability to describe the time-dependent  
16 behavior, a small Young's modulus was used to simulate static responses, and a large modulus  
17 had to be used to match the instantaneous responses associated with fast dynamic loading (e.g. 12  
18 MPa [22]; 5-50 MPa [33]).

19 In the 3D finite element analysis of the knee, fiber-composite and transverse isotropy have  
20 been considered for the menisci [22,34]. In a pioneer study of 3D knee model built on CT  
21 imaging, the menisci were considered as a nonhomogeneous solid reinforced by radial and  
22 circumferential collagen fibers [22]. This model was recently developed to include the 3D fiber  
23 structure of articular cartilage assuming random alignment for the tangential fibers in the

1 superficial zone [35]. Only elastic response was considered. The interplay of fibril  
2 reinforcement and fluid flow can not be investigated using these models.

3 Although there are sophisticated 3D knee models and improved cartilage models, a joint  
4 model combining the sophistication of both is yet to be developed. Based on our past studies on  
5 the transient load response of articular cartilage, it is particularly important to implement the fluid  
6 driven fibril reinforcement in the modeling. Understanding the role of collagen fibers in the  
7 mechanics of joints may also help understand cartilage degeneration leading to arthritis [13,36].  
8 Our long-term goal is to develop a 3D joint model using true contact geometry, incorporating  
9 realistic collagen orientations and cartilage thickness variations. Towards this greater goal, the  
10 objectives of the present study were (1) to test the ability of a fibril-reinforced model in  
11 simulating 3D anisotropic fluid pressurization, and (2) to develop a numerical procedure for  
12 implementing this model in 3D joint configurations. Idealized contact geometries were used for  
13 evaluation in this initial study. However, the numerical procedure is suitable for arbitrary contact  
14 geometries.

15

## 16 2. METHODS

17 Bone was considered rigid. Articular cartilage was modeled as a fluid-saturated porous matrix  
18 reinforced by a fibrillar matrix, using a previously developed fibril-reinforced model [16,17].  
19 The porous matrix was nonfibrillar, representing the solid matrix excluding the collagen fibers.  
20 The fibrillar matrix represented the collagen network; fiber orientation was in general a function  
21 of location, resulting in tissue anisotropy and inhomogeneity.

22 The nonfibrillar matrix was considered linearly elastic, defined by the Young's modulus  
23  $E_m$ , and Poisson's ratio  $\nu_m$ . The fibrillar matrix was assumed nonlinearly viscoelastic, direction  
24 and location dependent. Using  $\bar{x}$  to represent a fiber direction at a location with Cartesian

1 coordinates  $(X, Y, Z)$ , the fibrillar modulus in the direction of  $\bar{x}$  is a function of the tensile strain  
 2 in the direction,  $E_x^f(\varepsilon_x)$ , as well as a function of  $\bar{x}$  and  $(X, Y, Z)$  (anisotropic and  
 3 inhomogeneous). The fibrillar modulus was taken to be zero for compressive strains. The tensile  
 4 stress in the fibers can be determined using the hereditary integral [37] as

$$5 \quad \sigma_x^f(t) = \sigma_x^f(0) + \int_0^t G_x(t-\tau) E_x^f(\varepsilon_x) \dot{\varepsilon}_x d\tau, \quad (1)$$

6 where the relaxation function of the fibrillar matrix is represented by a discrete spectrum  
 7 approximation

$$8 \quad G_x(t) = 1 + \sum_m g_m \exp(-t / \lambda_m). \quad (2)$$

9 Here,  $\lambda_m$  are characteristic times for the viscoelastic dissipation, and  $g_m$  are dimensionless  
 10 constants.

11 Shear stress between parallel fibers was neglected, but shearing was modeled in the  
 12 nonfibrillar porous matrix. The subscript  $x$  in equations (1) and (2) can be replaced with  $y$  or  $z$  to  
 13 obtain the corresponding equations for  $\bar{y}$  or  $\bar{z}$  direction. This convention will be used  
 14 throughout the text to omit two sets of equations when appropriate. It is noted that  $\bar{x}$ ,  $\bar{y}$  and  $\bar{z}$   
 15 are functions of their location  $(X, Y, Z)$ .

16 The fibrillar stress can be calculated numerically as follows [17]

$$17 \quad \sigma_x^f(t + \Delta t) \approx \sigma_x^f(t) + G_x(\Delta t) E_x^f(\varepsilon_x) \Delta \varepsilon_x + \sum_m g_m [1 - \exp(\Delta t / \lambda_m)] \Psi_m^x(t + \Delta t), \quad (3)$$

18 where

$$19 \quad \Psi_m^x(t + \Delta t) \doteq \exp[-(t + \Delta t) / \lambda_m] \int_0^t \exp(\tau / \lambda_m) E_x^f(\varepsilon_x) \dot{\varepsilon}_x d\tau, \quad (4)$$

20 which is zero when  $t = 0$ . Here  $\varepsilon_x$  is evaluated at  $t$ , and  $\Delta \varepsilon_x = \varepsilon_x(t + \Delta t) - \varepsilon_x(t)$ . A numerical

21 approximation of equation (4) can be obtained as [17]

1  $\Psi_m^x(t + \Delta t) \approx \exp(-\Delta t / \lambda_m) \left[ \Psi_m^x(t) + E_x^f(\varepsilon_x)(\Delta \varepsilon_x)_{\text{prev}} \right],$  (5)

2 where  $(\Delta \varepsilon_x)_{\text{prev}} = \varepsilon_x(t) - \varepsilon_x(t_{\text{prev}})$ , and  $t_{\text{prev}}$  is the time one step prior to  $t$ . In other words, the  
 3 value in the square brackets of equation (5) is determined in the previous iterative step.

4 Using equation (8) from reference [17] to calculate the stress increment,  $\Delta \sigma_x$ , a new  
 5 equation can be derived as

6  $\frac{\partial \Delta \sigma_x}{\partial \Delta \varepsilon_x} \approx G_x(\Delta t) E_x^f(\varepsilon_x).$  (6)

7 The material model was implemented numerically using the USER MATERIAL option in  
 8 the commercial finite element package ABAQUS (Simulia Corp., Providence, USA). The user-  
 9 defined material model was introduced using a FORTRAN subroutine by defining the stress  
 10 tensor, and Jacobian matrix of the material,  $[D] = \partial \Delta \sigma / \partial \Delta \varepsilon$ . The stress in the solid is the sum  
 11 of the stress in the linearly elastic nonfibrillar matrix, and the normal stress determined by  
 12 equation (3). As a first step to test the 3D fibril-reinforced numerical model, only small  
 13 deformation problems were solved. Thus, the Jacobian matrix for the fibril reinforced solid  
 14 became

15  $[D] = \begin{bmatrix} D_{xx} & \lambda & \lambda & 0 & 0 & 0 \\ \lambda & D_{yy} & \lambda & 0 & 0 & 0 \\ \lambda & \lambda & D_{zz} & 0 & 0 & 0 \\ 0 & 0 & 0 & \mu & 0 & 0 \\ 0 & 0 & 0 & 0 & \mu & 0 \\ 0 & 0 & 0 & 0 & 0 & \mu \end{bmatrix},$  (7)

16 where  $\lambda$  and  $\mu$  are the Lamé constants of the nonfibrillar matrix,

17  $\lambda = \frac{E_m \nu_m}{(1 + \nu_m)(1 - 2\nu_m)},$  and  $\mu = \frac{E_m}{2(1 + \nu_m)}.$  (8)

1 The derivation of the Jacobian for the nonfibrillar matrix is standard, and thus is not shown.  
 2 Including the contribution of the fibrillar matrix to the Jacobian determined in equation (6), we  
 3 have

$$4 \quad D_{xx} = \lambda + 2\mu + G_x(\Delta t)E_x^f(\varepsilon_x). \quad (9)$$

5 Combining the user-defined material model with the built-in definition of hydraulic  
 6 permeability, a new porous media model for cartilage was made available. In our numerical  
 7 procedure, orthotropic properties were formulated with reference to the local Cartesian  
 8 coordinates at the element level,  $oxyz$ . This local frame of reference could be oriented in any  
 9 direction with the ORIENTATION option provided by ABAQUS, thus creating anisotropic  
 10 properties for the global  $OXYZ$  system.

11 In the general numerical model, both fluid-flow dependent and intrinsic viscoelastic behavior  
 12 were considered. The fluid-flow dependent viscoelasticity was modeled by the soil consolidation  
 13 procedure in ABAQUS with given permeabilities. The intrinsic viscoelasticity of the tissue was  
 14 modeled by the collagen viscoelasticity introduced by equations (1) and (2). Previous studies [17]  
 15 indicated that the fluid-flow dependent viscoelasticity alone could be used to approximate the  
 16 compressive load response of articular cartilage, provided that the instantaneous fibrillar modulus,  
 17  $G_x(0)E_x^f(\varepsilon_x)$ , was used in the calculations. In this case,  $G_x(t) \equiv G_x(0)$ , and equation (1) is  
 18 reduced to that for elastic stress. For the example problems with small deformation considered in  
 19 the present study, we simply took

$$20 \quad G_x(0)E_x^f(\varepsilon_x) = E_x^0 + E_x^\varepsilon \varepsilon_x \quad (10)$$

21 where  $E_x^0$  and  $E_x^\varepsilon$  are independent of strain, but dependent on  $\bar{x}$  and  $(X, Y, Z)$ . Note that these  
 22 parameters are for the instantaneous modulus of the fibrillar matrix, and thus are larger than those  
 23 for the static equilibrium modulus.

1 Unconfined compression and indentation testing were studied using the 3D finite element  
2 with the soil consolidation procedure in ABAQUS (Figs. 1 and 2). Ramp-compression and  
3 relaxation loading was applied. The compression amplitude was 0.02mm in all cases with strain  
4 rates ranging from 0.02%/s to 20%/s.

5 For the simulation of unconfined compression testing, a hypothetical cartilage disc was used.  
6 Fibers were assumed to be oriented in the X, Y and Z-directions with Z the depth direction. 432  
7 twenty-node hexahedral elements (C3D20RP) were meshed to represent a quarter of the disc (Fig.  
8 2a). For comparison, the problem was also solved for an axisymmetric configuration with 45  
9 eight-node quadratic elements (CAX8RP) (Fig. 2a). Fibers were assumed along the radial and  
10 circumferential ( $r$  &  $\theta$ ) directions to allow for axisymmetric modeling. Permeability was  
11 assumed to be isotropic to facilitate the comparison.

12 For simulating indentation testing, a piece of full-thickness cartilage from human medial  
13 femoral condyle was considered (Fig. 1). The split-line pattern [38] was used to determine the  
14 primary fiber orientations. Cartilage thickness was taken to be 2mm, in agreement with  
15 published values [39,40]. The cylindrical indenter was assumed to be impermeable and  
16 essentially rigid compared to the cartilage. Indentation was simulated as a mechanical contact  
17 between the articular surface of cartilage and the indenter, using the surface contact model in  
18 ABAQUS. Friction between the contact surfaces was neglected. 97,920 eight-node hexahedral  
19 elements (C3D8P) were meshed to represent the cartilage with 106191 nodes. A fine mesh was  
20 used in the vicinity of contact; a coarser mesh was used otherwise. For example, 18 elements in  
21 the depth or Z-direction were meshed, from 0.08mm-thick at the top to 0.18mm-thick at the  
22 bottom (Fig. 2b).

1 3. RESULTS

2 Selected results for the unconfined compression testing are shown in Figs. 3-4 for both  
3 axisymmetric and 3D finite element simulations. Conditions were identical for the axisymmetric  
4 and 3D calculations, except for fiber orientation. In the axisymmetric modeling, fibers were  
5 oriented in the radial, circumferential and depth ( $r$ ,  $\theta$  &  $Z$ ) directions; whereas in the 3D  
6 modeling, fibers were oriented in the  $X$ ,  $Y$  and  $Z$ -directions. The fibrillar modulus was assumed  
7 to be the same in three directions, and isotropic permeability was used. Alteration in fiber  
8 orientations produced some differences in reaction forces at moderate strain rates (not shown).  
9 These differences diminished at low strain rates ( $\leq 0.02\%/s$ ) or at very high compressive strain  
10 rates (1.3% difference in the reaction forces at the end of 2% compression applied at 20%/s, not  
11 shown).

12 For the case of 20%/s ramp compression and relaxation testing, the short and long-term  
13 deformations of the disc were essentially circular or axisymmetric, even though fiber orientation  
14 was in the  $X$  and  $Y$ -directions (Fig. 3). The greatest deviation from axisymmetric deformation  
15 occurred around 6s (Fig. 3). At 6s, the radial displacement at the disc periphery was  $11.3\mu\text{m}$  in  
16 the fiber ( $X$  &  $Y$ ) directions and  $7.9\mu\text{m}$  in the  $45^\circ$  oblique direction; it would be equally  $10.1\mu\text{m}$   
17 in all radial directions if fiber orientation was axisymmetric. In general, this deviation was more  
18 pronounced at early relaxation (Fig. 4).

19 Selected results of indentation of human knee cartilage (Figs. 1 and 2b) are shown in Figs. 5-  
20 8. Fluid pressure was highly localized in the contact region. Therefore, the rectangular tissue  
21 boundaries did not influence the results (the size of tissue meshed for analysis was sufficiently  
22 large). In a vertical plane, fluid pressure was essentially symmetric about the  $Z$ -axis at early  
23 times of relaxation (Fig. 5a). When the pressure further propagated from the contact surface to  
24 the deep zone, an asymmetric pattern was observed mainly in the surface layers (Fig. 5b),

1 reflecting the material anisotropy in that region, especially in the horizontal planes (Fig. 6). The  
2 impact of the  $-22^\circ$  and  $35^\circ$  fiber orientations could be clearly seen in Figs. 6a and 6c.  
3 Asymmetry was less significant in the deep zone due to lack of horizontal fibers there (Fig. 6b &  
4 d).

5 The impact of fiber orientations is best illustrated with the comparison of Figs. 6 and 7, for  
6 which all conditions were the same but fiber orientation. With all primary fibers oriented parallel  
7 in the  $x$ -direction (Fig. 7), the fluid pressure distribution was elliptical with axes aligned in the  
8 fiber directions. It is interesting that the short axis of a central ellipse aligned in the  $x$ -direction at  
9 short times (Fig. 7a), but in the  $y$ -direction at long times (Fig. 7c). This was probably because the  
10 high pressure at the early stage of loading tended to propagate in all directions but encountered  
11 higher resistance in the  $y$ -direction. As the fluid flowed preferably in the  $x$ -direction, the pressure  
12 pattern gradually changed. However, this mechanism needs to be confirmed with experimental  
13 observations and further analyses.

14 Fluid tended to flow in the fiber direction for the case of multiple fiber orientations (case of  
15 Fig. 1; results not shown) and for the case of a single fiber orientation (velocity vectors shown in  
16 Fig. 8). Naturally, fluid flow was also influenced by the contact boundary of the indenter that  
17 determined the fluid pressure boundary conditions. Therefore, not all fluid velocity vectors are  
18 aligned exactly in the fiber direction (Fig. 8).

19

#### 20 4. DISCUSSION

21 A fibril-reinforced model has been extended to account for arbitrary fiber orientation in  
22 articular cartilage, which made it possible to simulate the 3D anisotropic collagen network in a  
23 joint configuration. The proposed model was able to describe the 3D fiber direction dependent  
24 deformation (Figs. 3 & 4), fluid pressure (Figs. 5-7) and fluid flow (Fig. 8). It could also

1 simulate the strain-rate dependent load response (not shown), one of the important features of the  
2 mechanical response of articular cartilage that many models experienced difficulties to predict.

3 The 3D numerical procedure adapted from the axisymmetric modeling [17] produced  
4 reasonable results. The general methods for axisymmetric problems have been tested previously  
5 with experimental data obtained from several test configurations [16,17,20]. While the  
6 axisymmetric modeling is able to capture the overall or average load response of articular  
7 cartilage in vitro, the proposed 3D modeling can be used to describe anisotropic response of the  
8 tissue in situ (No swelling behavior was modeled in both cases).

9 A smaller permeability was used for the directions perpendicular to the fiber orientation.  
10 The permeability dependence on the fiber direction has not been well documented for articular  
11 cartilage. A smaller permeability in the direction parallel to the articular surface was obtained  
12 when both surface and some bottom layers were removed from the specimens [41]. Nearly  
13 isotropic permeability was directly measured at small static compressions [42]. These results  
14 were not particularly associated with fiber directions. In the lumbar annulus fibrosus, measured  
15 anisotropic permeability seemed to be related to the fiber direction [43]. Our assumption on the  
16 anisotropy of permeability was based on observations from ligaments and tendons, for which the  
17 permeability was found theoretically and experimentally to be smaller perpendicular compared to  
18 parallel to the fiber direction [44,45]. This was also considered to be true in articular cartilage in  
19 a recent mathematical study [46].

20 A large number of elements were used in the 3D indentation problem. Yet the system  
21 geometry was relatively simple compared with that of a whole joint contact. In a knee model  
22 based on CT images, a custom-designed program was used for the finite element analysis [22].  
23 The femoral, tibial and patellar cartilages were represented by 374 eight-node solid elements; the  
24 menisci were discretized into 424 eight-node solid elements reinforced by 1212 truss elements.

1 In the present study, the element size was much smaller to ensure spatial resolution for the small  
2 contact region in our indentation problem. Also, we used the eight-node elements, because the  
3 3D twenty-node elements in ABAQUS (version 6.4) experienced very slow convergence for  
4 contact problems (ABAQUS manual). However, a 3D eight-node element only approximates a  
5 constant fluid pressure within the element. Therefore, more elements were needed to  
6 approximate the pressure distributions well. Obviously, the time for the data preparation and  
7 computing of the 3D modeling increased enormously as compared to the axisymmetric modeling.

8 Stress concentrations were observed at the outer ring of the contact area where the indenter  
9 was subjected to a sharp change in shape. Similar effects were observed and investigated in  
10 axisymmetric modeling [21]. For indentation contact, the stress concentrations may need to be  
11 further investigated for the 3D configuration. However, this type of stress concentrations does  
12 not exist in an actual joint contact because geometrical changes there are subjected to smooth  
13 transitions. Therefore, this issue would not be a concern in the future whole joint contact studies.

14 In conclusion, an anisotropic material model of articular cartilage has been developed based  
15 on collagen orientation and the numerical procedure for the model has been evaluated. The  
16 results showed that the transient mechanical behaviors of cartilage were associated with collagen  
17 orientation. The direction dependence becomes less significant at low fluid velocity, which  
18 occurs during fast or nearly static compression. The proposed numerical procedure can be  
19 applied to whole joint contact mechanics with complex surface geometry, since the material  
20 model and numerical procedure are independent of boundary conditions. An extension of this  
21 study is to implement true contact geometry and realistic cartilage thickness variation into a joint  
22 model, in order to explore the implications of collagen fiber orientation in different physiological  
23 loading situations.

1 ACKNOWLEDGEMENTS

2 This study was partially supported by the Canadian Institutes of Health Research, the Canada  
3 Research Chair programme and the Croucher Foundation of Hong Kong, China. The finite  
4 element computation was performed on the WestGrid computers at the University of Calgary.

REFERENCES

- 1] Bader DL, Knight MM (2008) Biomechanical analysis of structural deformation in living cells. *Med Biol Eng Comput* 46: 951-963.
- 2] Mow VC, Kuei SC, Lai WM, Armstrong CG (1980) Biphasic creep and stress relaxation of articular cartilage in compression: theory and experiments. *J Biomech Eng* 102: 73-84.
- 3] Suh JK, Spilker RL (1994) Indentation analysis of biphasic articular cartilage: nonlinear phenomena under finite deformation. *J Biomech Eng* 116: 1-9.
- 4] Ateshian GA, Warden WH, Kim JJ, Grelsamer RP, Mow VC (1997) Finite deformation biphasic material properties of bovine articular cartilage from confined compression experiments. *J Biomechanics* 30: 1157-1164.
- 5] Mak AF (1986) Unconfined compression of hydrated viscoelastic tissues: a biphasic poroviscoelastic analysis. *Biorheology* 23: 371-383.
- 6] Suh JK, Bai S (1998) Finite element formulation of biphasic poroviscoelastic model for articular cartilage. *J Biomech Eng* 120: 195-201.
- 7] Cohen B, Lai WM, Mow VC (1998) A transversely isotropic biphasic model for unconfined compression of growth plate and chondroepiphysis. *J Biomech Eng* 120: 491-496.
- 8] García JJ, Altiero NJ, Haut RC (1998) An approach for the stress analysis of transversely isotropic biphasic cartilage under impact load. *J Biomech Eng* 120: 608-613.
- 9] Donzelli PS, Spilker RL, Ateshian GA, Mow VC (1999) Contact analysis of biphasic transversely isotropic cartilage layers and correlations with tissue failure. *J Biomech* 32: 1037-1047.
- 10] García JJ, Cortés DH (2007) A biphasic viscohyperelastic fibril-reinforced model for articular cartilage: formulation and comparison with experimental data. *J Biomech* 40: 1737-1744.

- 11] Mizrahi J, Maroudas A, Lanir Y, Ziv I, Webber TJ (1986) The “instantaneous” deformation of cartilage: effects of collagen fiber orientation and osmotic stress. *Biorheology* 23: 311-330.
- 12] Bassar PJ, Schneiderman R, Bank RA, Wachtel E, Maroudas A (1998) Mechanical properties of the collagen network in human articular cartilage as measured by osmotic stress technique. *Archives of Biochemistry and Biophysics* 351:207-219.
- 13] Aigner T, Stöve J (2003) Collagens – major component of the physiological cartilage matrix, major target of cartilage degeneration, major tool in cartilage repair. *Advanced Drug Delivery Reviews* 55: 1569-1593.
- 14] Brown, TD, Singerman, RJ (1986) Experimental determination of the linear biphasic constitutive coefficients of human fetal proximal femoral chondroepiphysis. *J Biomech* 19: 597-605.
- 15] Oloyede A, Flachsmann R, Broom ND (1992) The dramatic influence of loading velocity on the compressive response of articular cartilage. *Connective Tissue Research* 27: 211-244.
- 16] Li LP, Soulhat J, Buschmann MD, Shirazi-Adl A (1999) Nonlinear analysis of cartilage in unconfined ramp compression using a fibril reinforced poroelastic model. *Clinical Biomech* 14: 673-682.
- 17] Li LP, Herzog W (2004) The role of viscoelasticity of collagen fibers in articular cartilage: theory and numerical formulation. *Biorheology* 41: 181-194.
- 18] Korhonen RK, Laasanen MS, Töyräs J, Lappalainen R, Helminen HJ, Jurvelin JS (2003) Fibril reinforced poroelastic model predicts specifically mechanical behavior of normal, proteoglycan depleted and collagen degraded articular cartilage. *J Biomech* 36: 1373-1379.

- 19] Wilson W, van Donkelaar CC, van Rietbergen B, Ito K, Huiskes R (2004) Stresses in the local collagen network of articular cartilage: a poroviscoelastic fibril-reinforced finite element study. *J Biomech* 37: 357-366. Erratum 38: 2138-2140.
- 20] Li LP, Buschmann MD, Shirazi-Adl A (2003) Strain-rate dependent stiffness of articular cartilage in unconfined compression. *J Biomech Eng* 125: 161-168.
- 21] Li LP, Herzog W (2006) Arthroscopic Evaluation of Cartilage Degeneration using Indentation Testing - Influence of Indenter Geometry. *Clinical Biomechanics* 21: 420-426.
- 22] Bendjaballah MZ, Shirazi-Adl A, Zukor DJ (1995) Biomechanics of the human knee joint in compression: reconstruction, mesh generation and finite element analysis. *Knee* 2: 69-79.
- 23] Li G, Gil J, Kanamori A, Woo SL (1999) A validated three-dimensional computational model of a human knee joint. *J Biomech Eng* 121: 657-662.
- 24] Li G, Lopez O, Rubash H (2001) Variability of a three-dimensional finite element model constructed using magnetic resonance images of a knee for joint contact stress analysis. *J Biomech Eng* 123: 341-346.
- 25] Penrose JM, Holt GM, Beaugonin M, Hose DR (2002) Development of an accurate three-dimensional finite element knee model. *Comput Methods Biomech Biomed Eng* 5, 291-300.
- 26] Elias JJ, Cosgarea AJ (2007) Computational modeling: an alternative approach for investigating patellofemoral mechanics. *Sports medicine and arthroscopy review* 15: 89-94.
- 27] Ramaniraka NA, Terrier A, Theumann N, Siegrist O (2005) Effects of the posterior cruciate ligament reconstruction on the biomechanics of the knee joint: a finite element analysis. *Clinical Biomech* 20: 434-442.
- 28] Andriacchi TP, Briant PL, Bevill SL, Koo S (2006) Rotational changes at the knee after ACL injury cause cartilage thinning. *Clin Orthop Relat Res* 442: 39-44.

- 29] Haut Donahue TL, Hull ML, Rashid MM, Jacobs CR (2004) The sensitivity of tibiofemoral contact pressure to the size and shape of the lateral and medial menisci. *J Orthop Res* 22: 807-814.
- 30] Peña E, Calvo B, Martínez MA, Palanca D, Doblaré M (2005) Finite element analysis of the effect of meniscal tears and meniscectomies on human knee biomechanics. *Clinical Biomech* 20: 498-507.
- 31] Zielinska B, Donahue TL (2006) 3D finite element model of meniscectomy: changes in joint contact behavior. *J Biomech Eng* 128: 115-123.
- 32] Peña E, Calvo B, Martínez MA, Doblaré M (2007) Effect of the size and location of osteochondral defects in degenerative arthritis. A finite element simulation. *Comput Biol Med* 37: 376-387.
- 33] Yao J, Funkenbusch PD, Snibbe J, Maloney M, Lerner AL (2006) Sensitivities of medial meniscal motion and deformation to material properties of articular cartilage, meniscus and meniscal attachments using design of experiments methods. *J Biomech Eng* 128: 399-408.
- 34] Haut Donahue TL, Hull ML, Rashid MM, Jacobs CR (2003) How the stiffness of meniscal attachments and meniscal material properties affect tibio-femoral contact pressure computed using a validated finite element model of the human knee joint. *J Biomech* 36: 19-34.
- 35] Shirazi R, Shirazi-Adl A, Hurtig M (2008) Role of cartilage collagen fibrils networks in knee joint biomechanics under compression. *J Biomech* 41: 3340-3348.
- 36] Kuettner KE, Cole AA (2005) Cartilage degeneration in different human joints (review). *Osteoarthritis & Cartilage* 13: 93-103.
- 37] Fung YC (1993) *Biomechanics: Mechanical Properties of Living Tissues*, 2<sup>nd</sup> Edition, Springer-Verlag, New York.

- 38] Below S, Arnoczky SP, Dodds J, Kooima C, Walter N (2002) The split-line pattern of the distal femur: a consideration in the orientation of autologous cartilage grafts. *Arthroscopy: J Arthroscopic and Related Surgery* 18: 613-617.
- 39] Adam C, Eckstein F, Milz S, Putz R (1998) The distribution of cartilage thickness within the joints of the lower limb of elderly individuals. *J Anatomy* 193: 203-214.
- 40] Shepherd DET, Seedhom BB (1999) Thickness of human articular cartilage in joints of the lower limb. *Annals Rheumatic Diseases* 58: 27-34.
- 41] Jurvelin JS, Buschmann MD, Hunziker EB (2003) Mechanical anisotropy of the human knee articular cartilage in compression. *Proc. Instn Mech. Engrs, Part H, J Eng in Medicine* 217H: 215-219.
- 42] Reynaud B, Quinn TM (2006) Anisotropic hydraulic permeability in compressed articular cartilage. *J Biomechanics* 39: 131-137.
- 43] Gu WY, Mao XG, Foster RJ, Weidenbaum M, Mow VC, Rawlins BA (1999) The anisotropic hydraulic permeability of human lumbar annulus fibrosus. Influence of age, degeneration, direction, and water content. *Spine* 24: 2449–2455.
- 44] Chen CT, Malkus DS, Vanderby R Jr (1998) A fiber matrix model for interstitial fluid flow and permeability in ligaments and tendons. *Biorheology* 35:103-118.
- 45] Han S, Gemmell, SJ, Helmer KG, Grigg P, Wellen JW, Hoffman AH, Sotak CH (2000) Changes in ADC caused by tensile loading of rabbit Achilles tendon: evidence for water transport. *J Magnetic Resonance* 144: 217-227.
- 46] Federico S, Herzog W (2008) On the anisotropy and inhomogeneity of permeability in articular cartilage. *Biomechan Model Mechanobiol* 7: 367-378.
- 47] Woo SLY, Akeson WH, Jemmott, GF (1976) Measurements of nonhomogeneous, directional mechanical properties of articular cartilage in tension. *J Biomechanics* 9: 785-91.

Table 1 Material properties used in the finite element contact simulations shown in Figs. 5-8. The Young's modulus and Poisson's ratio for the indenter were taken to be 200 GPa and 0.3 respectively. The fibrillar properties were determined with reference to our previous axisymmetric modeling. The ratio of moduli in  $y$ -direction versus  $x$ -direction was taken to approximate the tensile test data [47]

Layer	Elements in depth direction (Fig. 2b)	Instantaneous Fibrillar Moduli (MPa)			Nonfibrillar Porous Matrix		Permeability ( $10^{-3}\text{mm}^4/\text{Ns}$ )		
		$x$ *	$y$	$z$	$E_m$ (MPa)	$\nu_m$	$x$	$y$	$z$
Upper 0.64 mm	8	$6+3200\varepsilon_x$	$1.8+960\varepsilon_y$	0	0.20	0.30	3	1	1
Mid 0.70 mm	6	$3+1600\varepsilon_x$	$0.9+480\varepsilon_y$	0	0.26	0.36	2	1	1
Deep 0.66 mm	4	0	0	0	0.32	0.42	1	1	1

\* These refer to the local  $x$ ,  $y$  and  $z$  directions with respect to the element. The  $x$ -axis corresponds to the primary collagen orientation.

## FIGURE CAPTIONS

Fig. 1 Primary collagen orientations of a piece of articular cartilage (lower figure, zoomed) located on a distal femur (upper figure). Four different fiber orientations were considered as shown with A, B, C and D zones (adapted from the split-lines in [38]). The size of the tissue considered is  $14 \times 10 \times 2$  mm with 2 mm in the depth or  $z$  direction. The indenter shown with the dotted circle has a diameter of 2 mm.

Fig. 2 Finite element meshes for the simulations of (a) unconfined compression and (b) indentation. For clarity of the figure, only meshes in the  $XZ$  plane are shown. For the case of unconfined compression, the mesh for the 3D modeling in the  $XZ$  plane is actually the same as that for the axisymmetric modeling (showing half cartilage thickness). For the case of indentation, the mesh is symmetric about  $XZ$  and  $YZ$  planes.

Fig. 3 Radial displacement of the disc periphery for time at 0.1, 6 and 200s (only a quarter of the disc is shown). Here, 2% compression was applied in 0.1s. The solid lines show the displacements obtained from the 3D mesh; they are essentially circular except the one for  $t = 6$ s. The dotted line shows the displacement obtained from the axisymmetric mesh (Fig. 2a) for  $t = 6$ s. The Young's modulus of the fibrillar matrix was considered identical in the  $X$  and  $Y$  (3D) or  $r$  and  $\theta$  (axisymmetric) directions,  $G(0)E_f = (3+1600\varepsilon)$  MPa, where  $\varepsilon$  is the fibrillar strain. The nonfibrillar properties were  $E_m = 0.26$  MPa,  $\nu_m = 0.36$ , permeability  $k \equiv 0.003$  mm<sup>4</sup>/Ns.

Fig. 4 Radial displacement at the disc periphery as a function of time for the case shown in Fig. 3, indicating the radius changes at given directions. The solid line shows the radius change in fiber directions, or  $X$  and  $Y$  directions; the line marked as "45° oblique" indicates the radius change in the direction 45° from  $X$  or  $Y$ -axis; these were obtained from the 3D mesh. The result from axisymmetric mesh is shown for comparison.

Fig. 5 Fluid pressure (kPa) distributions in the vertical XZ-plane for the case shown in Fig. 1, a) for time  $t = 20$ s and b) for time  $t = 100$ s. 1% compression was applied in 1s. The vicinity of contact of 3.5 mm wide with full cartilage thickness is shown. The material properties are listed in Table 1.

Fig. 6 Fluid pressure (kPa) distributions in the two horizontal planes indicated in Fig. 5a,  $z = 0.4$  and 1.5mm, for times  $t = 20$  and 100s. The area shown is  $3.5 \times 3.5 \text{ mm}^2$  (element mesh  $28 \times 28$ ). Figure d) also shows the indenter position with the broken line. Note that the two upper figures share one legend, and the two lower figures share another. The material properties are listed in Table 1.

Fig. 7 Fluid pressure (kPa) distributions in the two horizontal planes, as compared to those in Fig. 6, while primary collagen orientations were all assumed to be in  $-22^\circ$  direction in the present case. The  $x$ -direction in figure a shows the primary fiber orientation.

Fig. 8 Fluid velocity at the depth of 0.4mm for time at 20s, for the indentation problem shown in Fig. 1. However, in this case, all collagen orientations were assumed to be in  $-22^\circ$  direction, and a larger indenter with a diameter of 3.5mm was used, as indicated with the circle. Only the central area of  $5.0 \times 5.0 \text{ mm}^2$  is shown (element mesh  $40 \times 40$ , represented by the dots). The maximum velocity was  $7.24 \times 10^{-5} \text{ mm/s}$ . For clarity of the figure, velocity vectors of magnitude smaller than half maximum are not shown. The material properties are listed in Table 1.

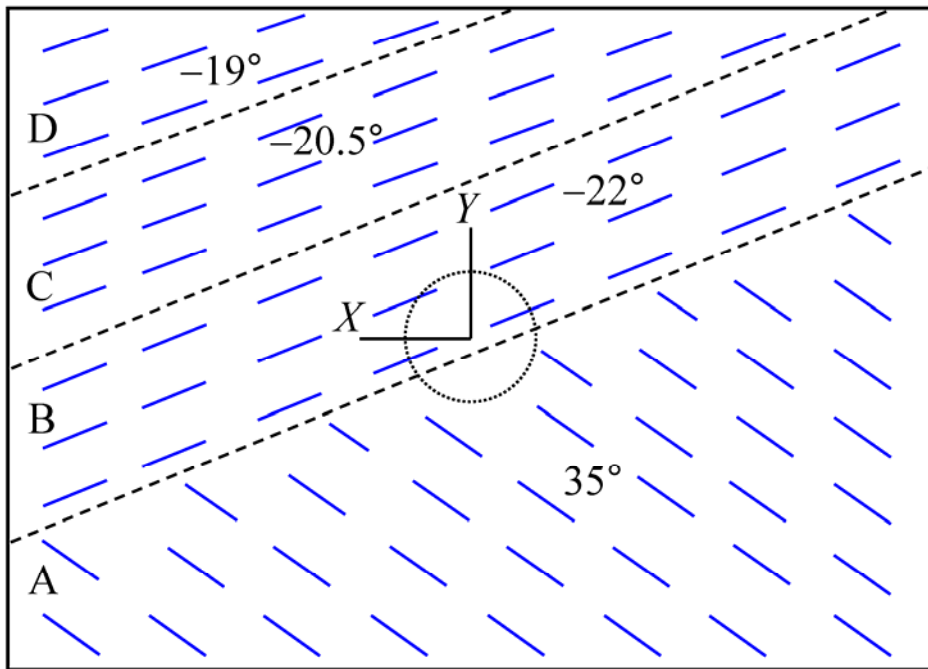
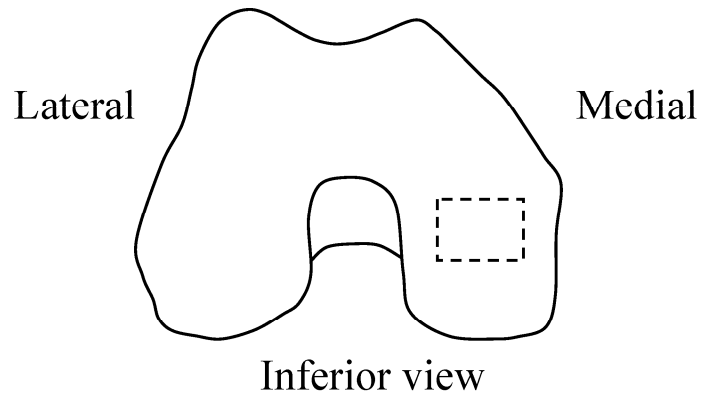


Figure 1

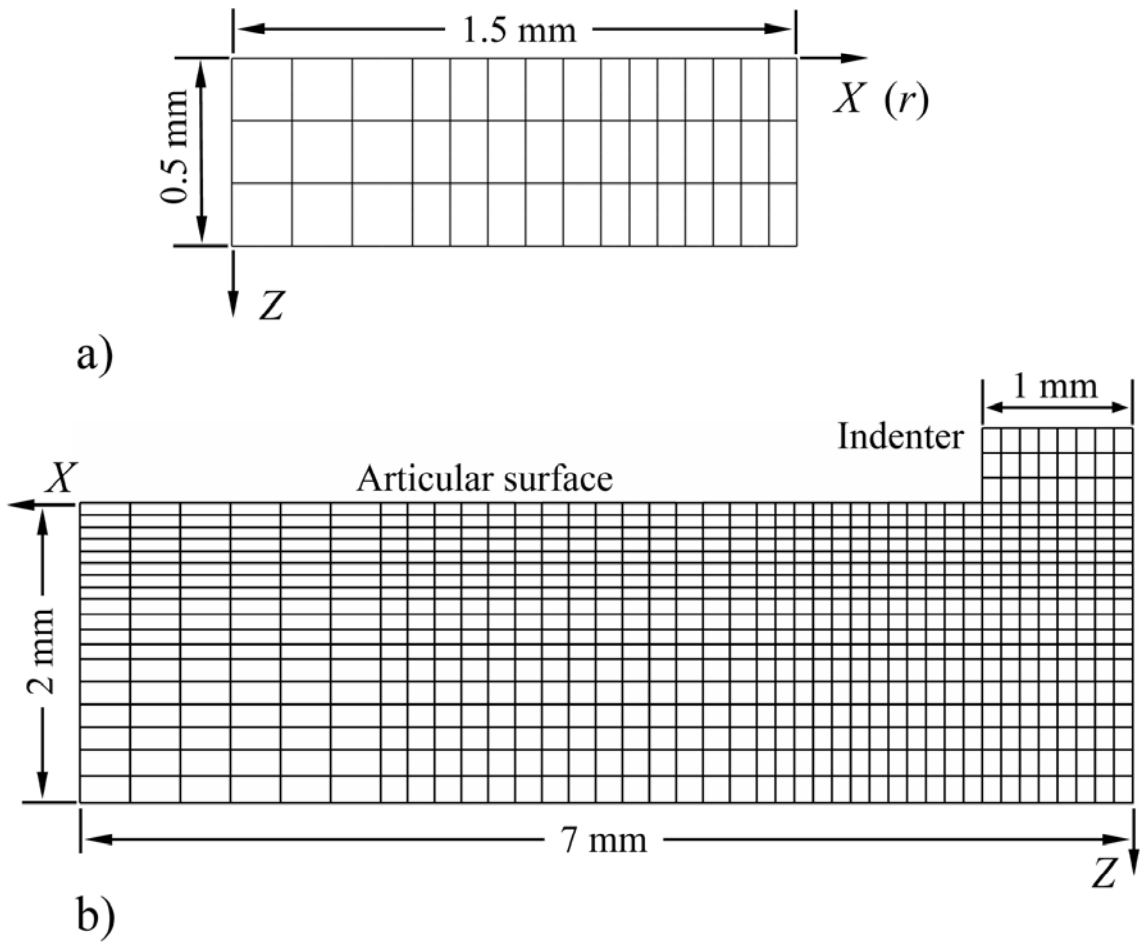


Figure 2

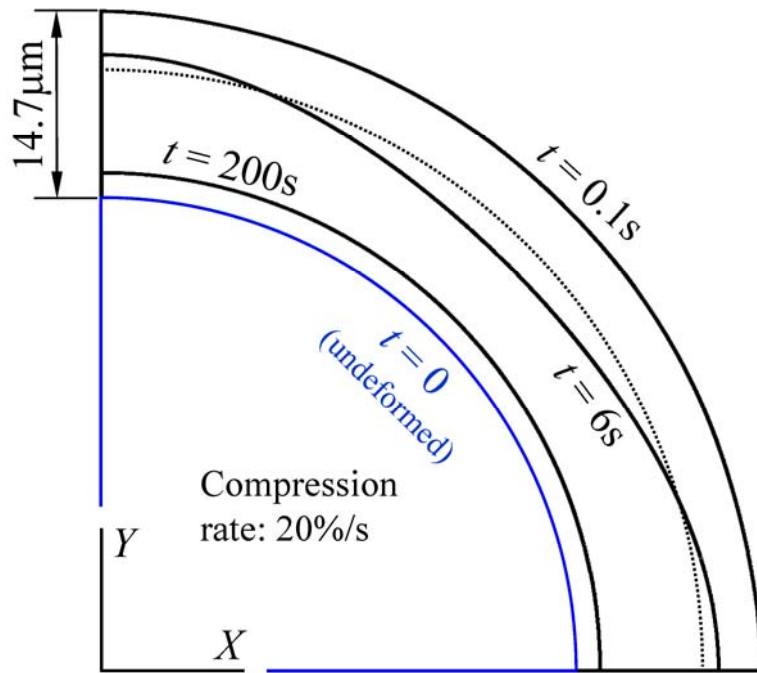


Figure 3

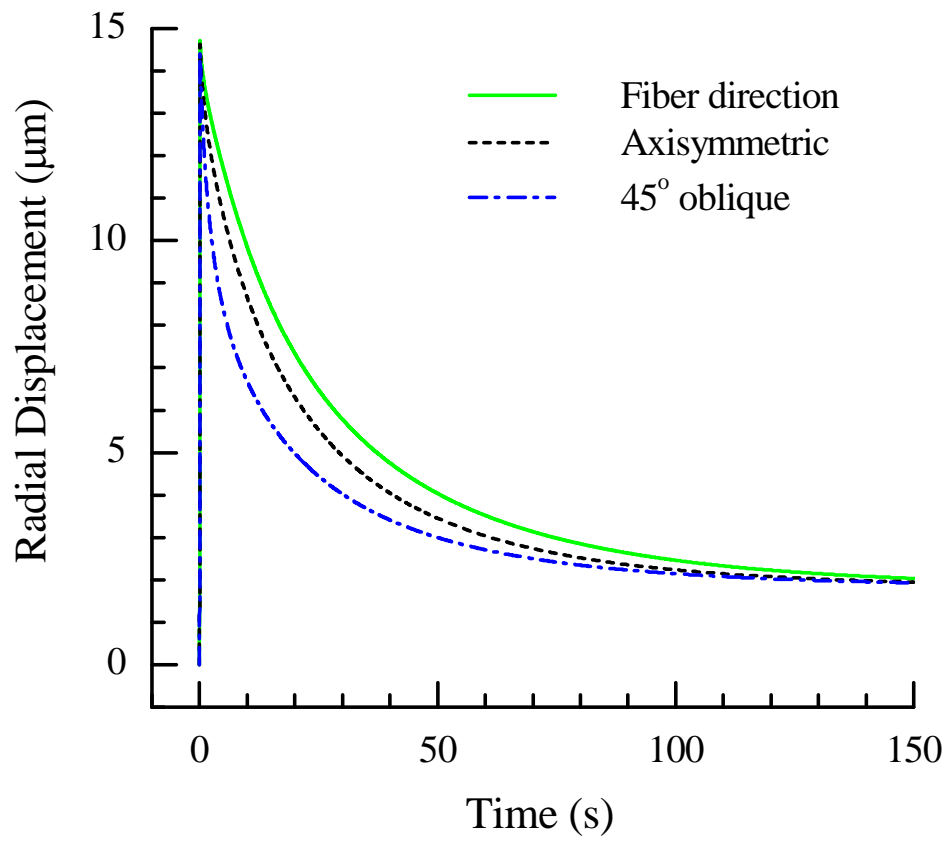


Figure 4

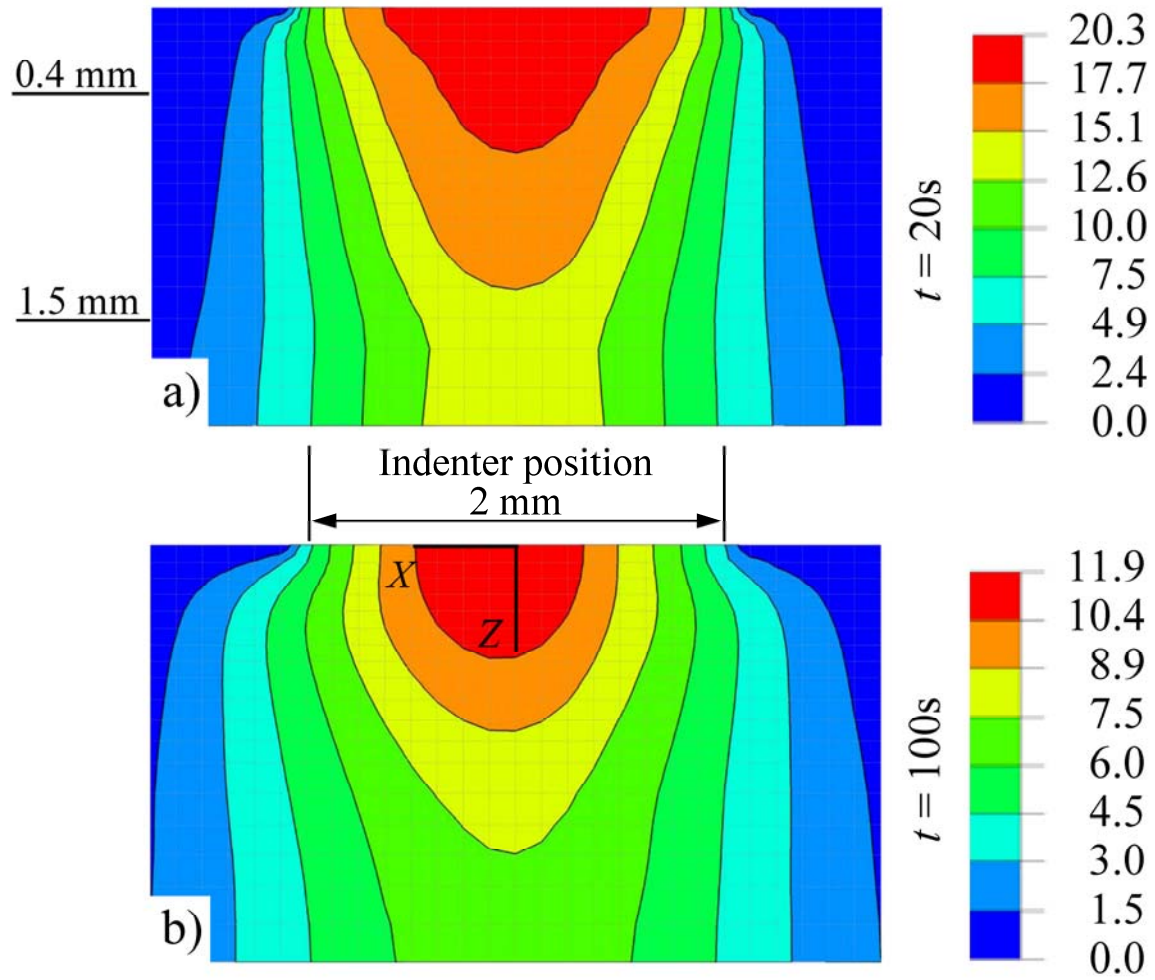


Figure 5

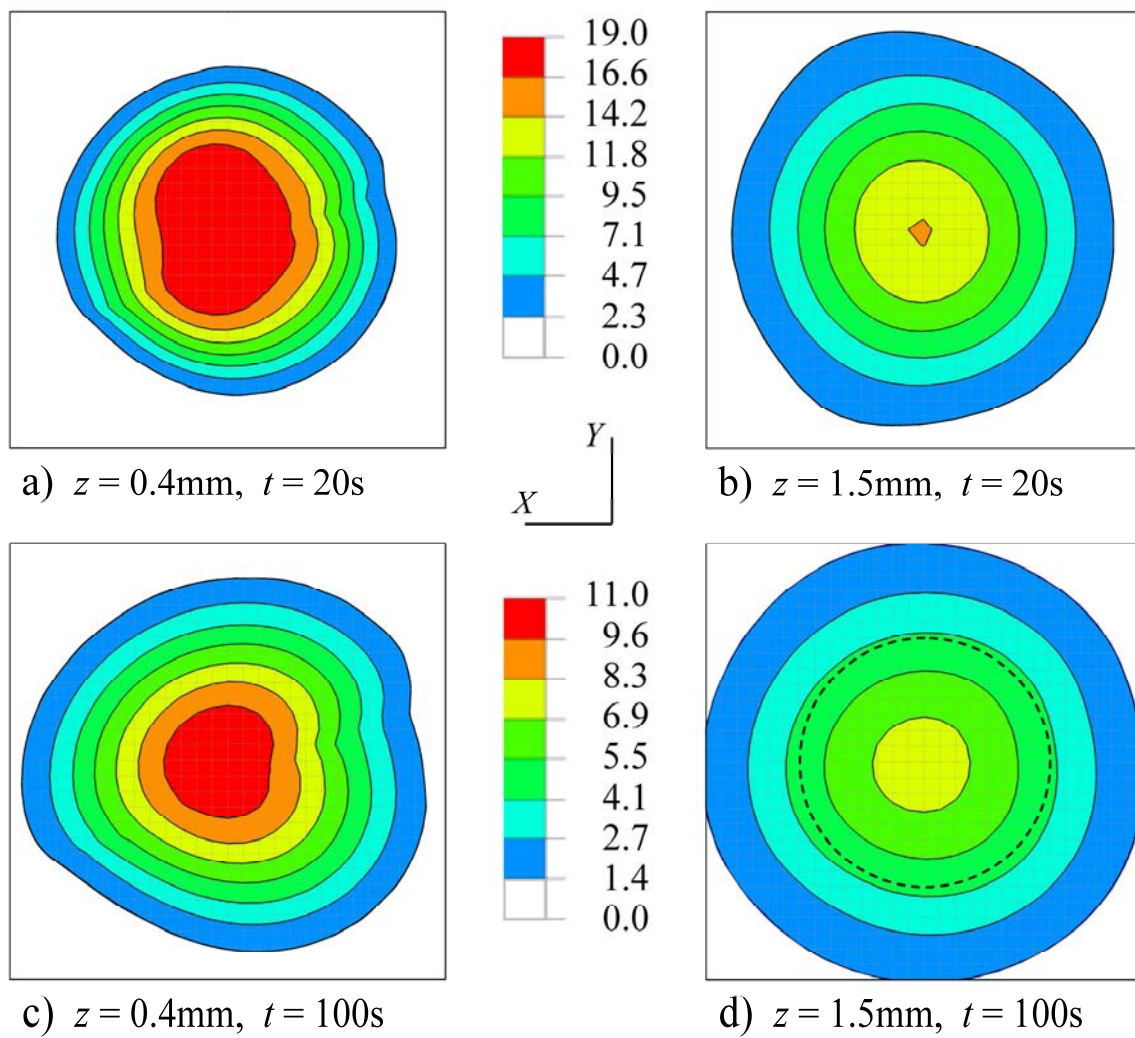


Figure 6

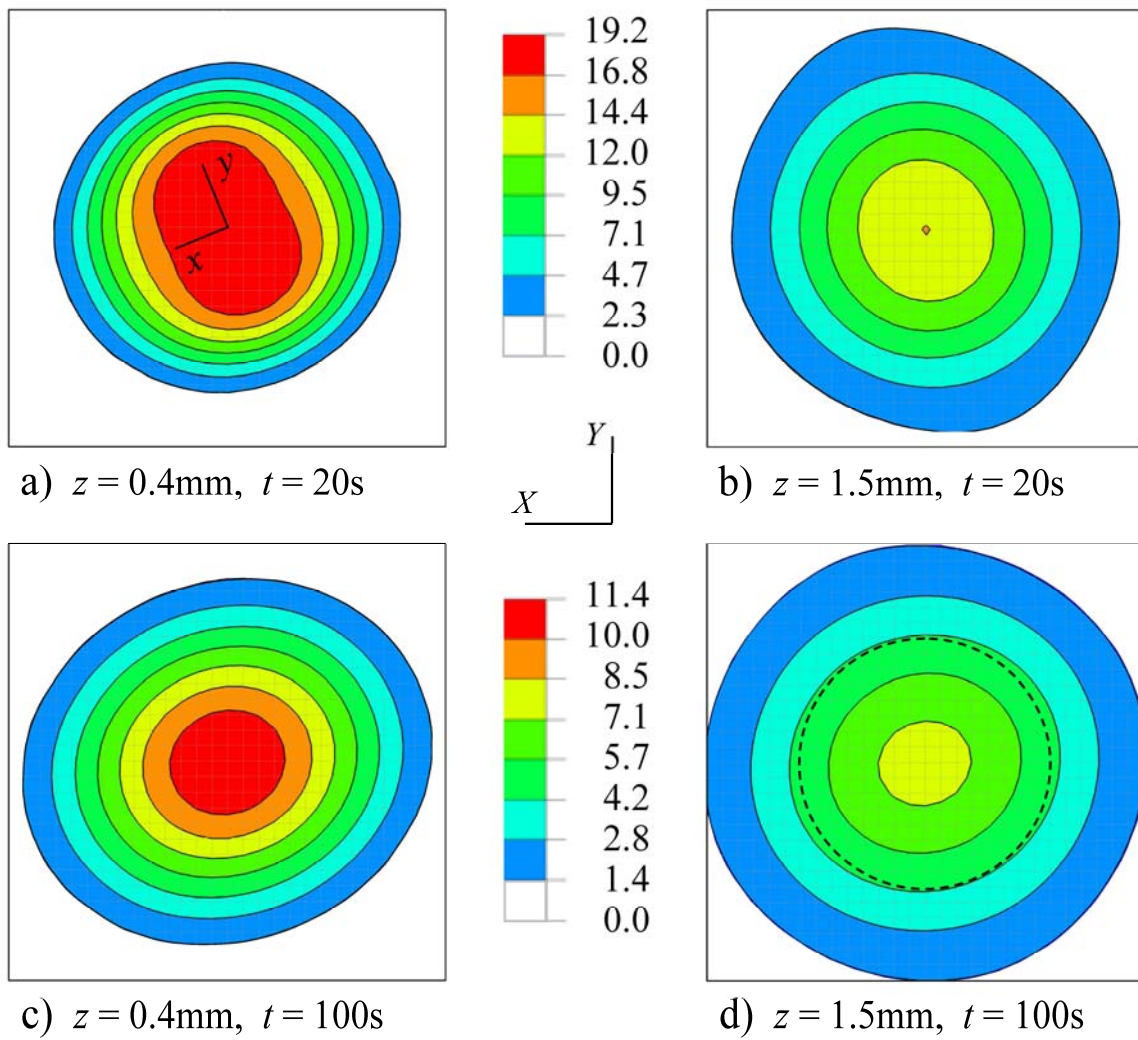


Figure 7

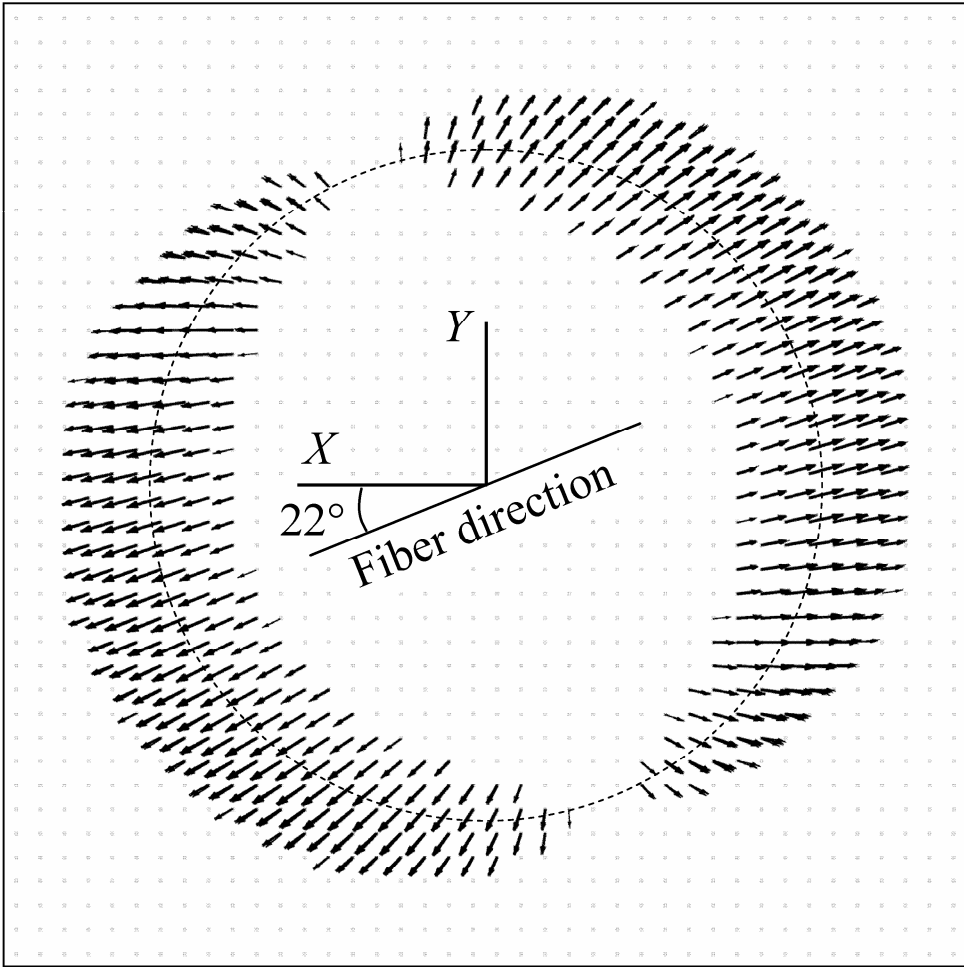


Figure 8